RESEARCH ARTICLE

# An optimised cell for *in situ* XAS of gas diffusion electrocatalyst electrodes

Connor Sherwin,[a, b, c] Veronica Celorrio,*[b] Ursa Podbevsek,[c] Katie Rigg,[c] Toby Hodges,[c] Armando Ibraliu,[b, e] Abbey J. Telfer,[b, d] Lucy McLeod,[c] Alessandro Difilippo,[c] Elena C. Corbos,[c] Chris Zalitis,[c] Andrea E. Russell*[a]

[a] C. Sherwin, Prof. A. E. Russell
Department of Chemistry
University of Southampton
Southampton, SO17 1BJ (United Kingdom)
E-mail: A.E.Russell@soton.ac.uk

[b] C. Sherwin, Dr. V. Celorrio, A. Telfer, A. Ibraliu
Diamond Light Source Ltd
Didcot, OX11 0DE (United Kingdom)
E-mail: Veronica.Celorrio@diamond.ac.uk

[c] C. Sherwin, Dr. E. C. Corbos, A. Difilippo, T. Hodges, Dr. U. Podbevsek, Dr. L. McLeod, K. Rigg, Dr. C. Zalitis
Johnson Matthey Technology Centre
Reading, RG4 9NH (United Kingdom)

[d] A. J.Telfer
Department of Chemistry
University of York
York, YO10 5DD (United Kingdom)

[e] A. Ibraliu
Department of Chemistry Engineering
University of Manchester
Manchester, M13 9PL (United Kingdom)

Supporting information for this article is given via a link at the end of the document.

**Abstract:** The quality of *in situ* XAS of electrochemical systems is highly sensitive to electrode disturbances, such as gas evolution and gas consumption at an electrolyte / catalyst interface. A novel *in situ* spectro-electrochemical X-ray absorption spectroscopy (SPEC-XAS) cell is presented as a new tool for the characterisation of gas evolving and consuming electrocatalysts at high overpotentials. By utilising a thin, porous membrane with efficient electrolyte and gas circulating loops, an improved three phase interface is established that enabled efficient gas supply and minimised the interference from bubble formation. X-ray absorption spectroscopy (XAS) measurements were conducted in fluorescence mode with three experiments selected to demonstrate the cell's performance. The first two reactions; an in-situ study of a highly active amorphous iridium oxide catalyst during the oxygen evolution reaction (OER) and an in-situ study of copper oxide during the carbon dioxide reduction reaction ($CO_2$RR) are used to exemplify the XAS data quality achieved under operational conditions. Thirdly, a detailed XAS investigation of a highly dispersed platinum catalyst during the oxygen reduction reaction (ORR) is presented, along with comparative data in nitrogen. These measurements show the retention of oxygen on the surface of the platinum metal particles down to 0.48 V (vs. RHE), well below the platinum oxide reduction peak.

## Introduction

Electrocatalytic reactions that produce gas phase products (gas evolving) or require gas phase access of the reactant (gas consuming) represent an important research area for the future chemicals and fuels for grid balancing and energy storage applications. Such reactions include the oxygen evolution reaction (OER), oxygen reduction reaction (ORR) and $CO_2$ reduction reaction ($CO_2$RR) to form hydrocarbons. The first two are the fundamental reactions occurring at the anode of proton exchange membrane water electrolysers (PEMWEs) and the cathode of proton exchange membrane fuel cells (PEMFCs). Both represent vital technologies in the transition to renewable energy storage and conversion. For PEMWEs, iridium oxides are the preferred anode catalyst, displaying the best combination of high activity and stability.[1-3] While for PEMFCs highly dispersed platinum catalysts have been the most widely used anode and cathode material.[4-5] The carbon dioxide reduction reaction is an important emerging technology in tackling anthropogenic $CO_2$ because of its ability to create value-added chemicals.[6-7] Copper based catalysts remain one of the only materials capable of producing $C_{2+}$ products and are therefore at the forefront of much research.[8]

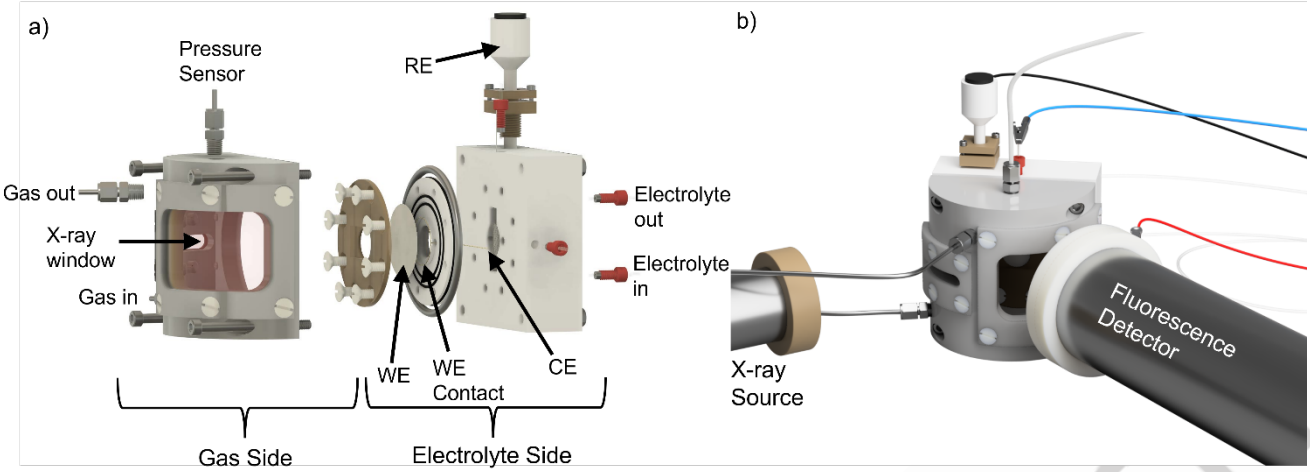


**Figure 1** a) Exploded view of the cell showing the working electrode (WE), counter electrode (CE), reference electrode (RE) placement. The large Kapton X-ray windows allow measurement at varying X-ray incident angles and a large area of fluorescence detection. b) the assembled cell showing all electrical and gas connections to the cell and the position of the X-ray source and detector.

Detailed understanding of the structure and chemistry of the electrocatalysts during operation at high current densities is essential to understand the catalytically active state and to enable the study of the degradation properties of the materials at the limits of their operation. X-ray absorption spectroscopy (XAS) has widely been applied to the study of these reactions because of its ability to provide information regarding the oxidation state and local coordination in realistic working environments.

The development of a cell capable of maintaining a constant working environment is important for reliable and consistent XAS measurements. The use of gas diffusion electrodes (GDEs) for *in situ* XAS of gas consuming reactions has been reported extensively, especially for fuel cell catalysts, and the $CO_2$RR, as well for other *in situ* techniques.[9-13] Previous cell strategies have employed flow cell designs, as this helps to maintain high mass transport conditions and prevent local electrolyte heating due to the high intensity X-ray beam.[14-16] Burnett. et al. developed an adapted version of Wise et al.'s flow cell, with a larger outlet tubing to prevent bubbles blocking the electrode connections.[16-17] In Burnett et al.'s setup, the highest applied potential reached during OER testing was 1.78 V, without *iR* correction.[17] While no activity data during XAS measurements were published, this setup still suffered with interference from bubbles and the non-ideal cell geometry likely contributes to a large *iR* drop at such high overpotentials. Carbon substrates were also used which will passivate and form a resistive layer reducing the electrochemical accessibility of the bound catalyst, further adding to the uncertainty when at such high overpotentials. Binninger et al. also developed a flow cell where, to tackle the problem of bubbles and gas solubility in liquid electrolyte, they degassed the electrolyte.[14] This, however, still limits gas consuming reactions to the solubility of the gas in the electrolyte and can only partially tackle the problem with bubbles forming during gas evolving reactions, with Diklić et al. reporting *in situ* data up to a mass activity around 0.130 A $mg^{-1}$ in this cell.[18-19] Further development of electrochemical XAS cells aim to improve the intrinsic kinetic activity at the relevant overpotentials during XAS measurements. This means more of the catalyst layer is contributing to the active state of the material in the XAS spectra, resulting in a more realistic understanding of the active catalyst under relevant conditions. Moving to a membrane electrode assembly (MEA) fuel cell, while providing the most realistic operating environment, it leads to problems with absorption from the side of the MEA not under investigation and difficulty in the positioning of the reference electrode (when they are used), meaning it is hard to accurately measure the voltage of the working electrode.[9, 12, 20] Additionally, using an *in situ* water electrolyser cell has the added difficulty of water attenuation of the catalyst layer. Using a single MEA design for measuring both gas consuming and gas evolving reactions is therefore much more problematic.

In the work described herein, we present a new design for an *in situ* spectro-electrochemical X-ray absorption spectroscopy (SPEC-XAS) cell that has been optimised to enable the characterisation of gas evolving and consuming electrocatalysts. The improved three-phase interface compared to earlier XAS cell designs allows characterisation of electrocatalysts at higher current densities than previously reported.[14, 18-19] A porous hydrophobic membrane onto which the electrode material of interest is deposited (similar to the floating electrode) is mounted into the cell with a pulse-free flowing electrolyte and gas flow path to allow improved mass transport in both the gas consuming and evolving configurations.[21] Utilising GDEs to improve gas management during *in situ* XAS measurements during the OER is shown here to improve the operating current densities achieved.

The use of a SPEC-XAS cell is exemplified in the study reported here for gas evolving and consuming reactions through the investigation of highly active amorphous iridium oxide during the OER and the analysis of copper oxide during the $CO_2$RR. Additionally, a detailed XAS study of highly dispersed platinum during the ORR is presented. Together these three studies demonstrate the scope and possible applications of the SPEC-XAS cell for characterising electrocatalysts used for a wide range of gas evolving and/or consuming electrocatalytic reactions.

## Cell Design

The SPEC-XAS cell was designed to have two main compartments split by a GDE (full schematics shown in Figure S1); the electrolyte side where the electrolyte is contained and electrochemistry occurs, and the gas side where gasses are exchanged and the X-rays are incident on the electrode (Figure 1a & b). On the electrolyte side, the flow channel was designed to have a small total volume of approximately 7 ml to allow a fast flow (5-15 ml $min^{-1}$) to remove any bubbles that are formed when studying a gas evolving reaction. The reference electrode is placed in a separate channel 6 mm from the working electrode for low uncompensated resistance to allow accurate *iR* correction (0.75 Ω for a 100 nm Au layer in 1 M $H_2SO_4$, Figure S4). By separating the electrolyte and X-ray sides of the cell and measuring fluorescence XAS instead of transmission (in the current setup transmission is not possible), the requirement to minimise the thickness of the electrolyte in the X-ray beam through path is removed, which means the counter electrode can be positioned directly in front of the working electrode ensuring an even current distribution.

On the gas side of the cell, a hemicylindrical design was chosen (275 ml) which allows the X-ray incidence angles to be tuned between 15° and 60° (Figure S2). This compartment can be supplied with reactant gas when studying gas consuming reactions or purged with inert gas for gas evolving measurements. Using shallow incidence angles increases the fluorescence signal by up to 3.3 fold, meaning the electrode loadings can be significantly reduced.

The working electrode consisted of a PTFE membrane sputtered with Au or Pd to serve as the current collector, this is then coated with the catalyst of interest. The PTFE membrane was used as a GDE to transport gas towards (gas consuming electrode) or away (gas evolving electrode) from the catalyst to allow high geometric current densities to be achieved, see relevant reactions below (200 mA $cm^{-2}$ demonstrated, although a limit was not reached), Figure 8. Fluorescence XAS requires a loading around 0.2 $mg_{metal}$ $cm^{-2}$ for a reasonable edge step (actual loadings given for each experiment below), which is significant enough to introduce catalyst layer effects which will inevitably lead to a compromise between XAS measurements and the catalysts intrinsic performance.

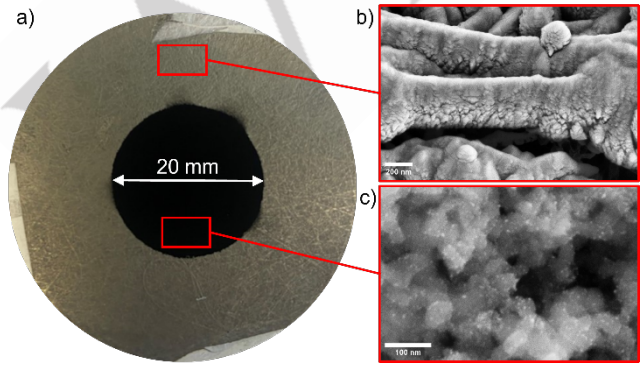


**Figure 2** a) Photograph of the Pd coated PTFE electrode with the 50% Pt/C spray coated to a 20 mm diameter in the centre. SEM images show the top-down view of the Pd coated PTFE (b) and Pt/C coated Pd/PTFE (c) regions.

For the iridium and copper edge measurements a Au current collector was used, as the Ir $L_{III}$ and Au $L_{III}$ edges are separated by 704 eV, yielding a k range of 13.3, sufficient for multiple shell EXAFS (extended X-ray absorption fine structure) fits. On the other hand, the Cu K edge is 2940 eV lower than the Au $L_{III}$ absorption edge, hence there is no problem using Au. A Pd current collector was used for measurements at the Pt edge as the Pt $L_{III}$ and Au $L_{III}$ only have a 355 eV separation, whereas Pd has no absorption edges near the Pt $L_{III}$ edge. Au works well as a current collector for OER measurements as it is stable against corrosion in the experiment timeframe, in contrast to previous cell designs which used a carbon substrate.[17] Figure 2 shows a photograph of an electrode used for ORR testing of Pt/C with a 100 nm Pd current collector coated by physical vapour deposition (PVD). SEM of this region (Figure 2b) shows an even coverage of the surface and the high porosity of the electrodes arising from the fibrous nature of the membrane. Figure 2c shows the highly dispersed platinum on carbon layer of the electrode created by spray coating the catalyst ink. The small particle size and high dispersion of the platinum is demonstrated in this image with an average particle size around 2 nm (determined by TEM, Figure S16).

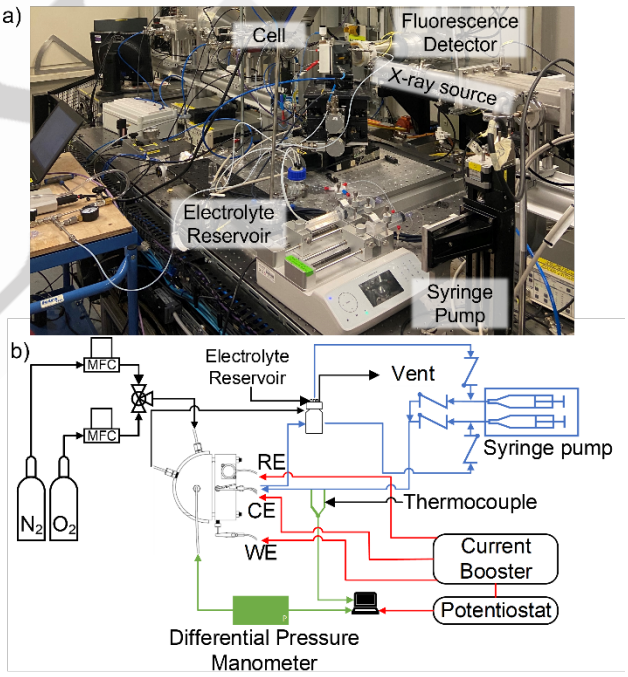


**Figure 3** a) View of the cell on B18 at Diamond Light Source b) schematic representation of all the connections made to the cell during XAS measurements.

A view of the full setup and a schematic showing the connections to the cell are shown in Figure 3. A syringe pump was used to avoid oscillations occurring in the EXAFS by preventing any pulsing of the working electrode during XAS measurements (comparison of the effects of different pumps on the XAS data is shown in Figure S3). Flowing the electrolyte and gasses maintains high mass transport conditions and prevents bubble formation from causing oscillations in the XAS data. A differential

pressure sensor was used to ensure a constant gas pressure was maintained throughout the experiments. This sensor can also give an indication of electrode flooding or a blockage. For gas consuming reactions a single gas line from the cell outlet was used to purge the electrolyte reservoir. However, during gas evolving reactions two gas connections are preferable; one to purge the gas side of the cell and another to separately purge the electrolyte reservoir. This reduces the electrolyte saturation with the evolved products.

## Results and Discussion

### OER on Iridium Oxide

The OER is an important reaction for understanding electrolyser performance. We have chosen this reaction to exemplify XAS data quality during gas evolution where higher potentials and current densities are required for realistic insights into the catalyst performance. Figure 4 shows an OER activity comparison of a commercial iridium oxide (Alfa Aesar, Premion$^{TM}$) in different electrochemical setups. The floating electrode (FE) technique offers an almost idyllic mass transport regime which utilises ultra-low catalyst loadings to create very thin catalyst layers and the optimised pore geometries are established by using PCTE membranes.[21-22] The FE therefore provides a benchmark for the intrinsic catalyst performance from which the SPEC-XAS cell can be compared. Whilst, the SPEC-XAS cell comprises elements from this technique, using a Au current collector coated onto porous membranes to avoid oxidation of the substrate at high potentials, higher loadings (typically around 0.2 $mg_{metal}$ $cm^{-2}$ (0.19 $mg_{Ir}$ $cm^{-2}$ used here), an order of magnitude higher than the FE) are required for XAS studies. This results in thicker catalyst layers generating layer effects. A comparison of the SPEC-XAS and FE mass normalised cyclic voltammograms (CVs) (Figure S6), shows a small drop in the CV area due to the high degree of catalyst utilisation in the FE. Flowing the electrolyte also helps to improve the mass transport by removal of gas bubbles from the working electrode and supplying fresh electrolyte to the catalyst.

Comparison of the linear sweep voltammograms (LSVs) for the different electrochemical cell types shows the intermediate performance of the SPEC-XAS cell compared to the FE. While it is hard matching the performance of the FE in its entirety due to the trade off in loading needed for good XAS measurements, the performance overlaps up to 1.52 V vs. RHE. In this kinetic controlled region of the LSV the FE and SPEC-XAS cell demonstrate similar Tafel slopes of 65 and 71 mV $dec^{-1}$ respectively, similar to that published by Reier et al.[23] After this, the catalyst enters a mixed mass transport kinetic region, making the actual voltage difficult to determine due to layer effects, but no mass transport limitation was observed up to 4.2 mA $cm^{-2}_{geo}$ (Figure S5). This mixed mass transport kinetic region is also observed in electrolyser catalyst coated membranes (CCMs), with Bernt and Gasteiger showing *iR* corrected polarisation curves up to ~1.6 $V_{iR\ Free}$ while their voltage loss breakdown shows the OER overpotential doesn't increase much above 1.52 $V_{iR\ Free}$ at 3 A $cm^{-2}$.[3, 24]

Some limitations in the setup remain, namely the higher loadings, the highly porous and rough PTFE creating a lateral resistance over the electrode, and the large catalyst geometric area (π $cm^{-2}$). The higher loadings are required for a reasonable edge step, however as discussed above, improvements could be made by reducing the X-ray incidence angle. The lateral resistance could be improved through using PTFE treated PCTE membranes similar to the FE. Finally, the geometric areas could be reduced based on the X-ray beam size and the number of different points measured over the electrode.

When comparing the data reported here to the I-V curves of PEMWE set-ups, the OER mass activity observed in the SPEC-XAS cell is in good agreement over the full range of working potentials (after correcting for the temperature difference). For example, Bernt et al. presents an I-V curve reaching around 0.47 A $cm^{-2}$ at an overpotential of 0.32 (equal to 1.50 $V_{iR\ Free}$) and at a temperature of 80 °C.[24] With an anode loading of 2.00 $mg_{Ir}$ $cm^{-2}$, this corresponds to a mass activity of 0.24 A $mg_{Ir}^{-1}$. Using the SPEC-XAS cell we report a mass activity of 0.013 A $mg_{Ir}^{-1}$ at 25 °C. Correcting the temperature to 80 °C (calculation shown in Supporting Information S2), as is typical for PEMWE operation, the mass activity obtained is around 0.15-0.19 A $mg_{Ir}^{-1}$.

Stable currents are recordable even at high voltages and with high current densities (Figure S7) showing the effective management of bubbles during the OER. This efficient gas circulation system is evident from the quality of the EXAFS recordable at these high potentials, showing a high signal to noise ratio (Figure S10).

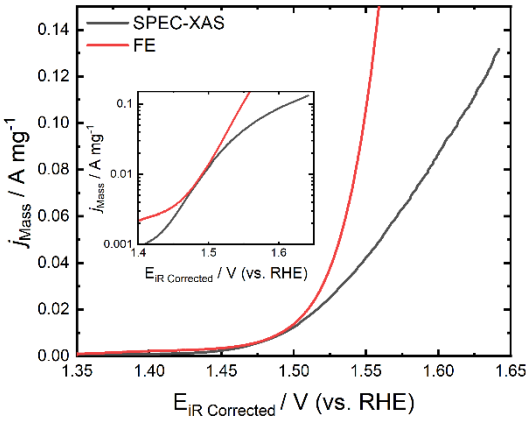


**Figure 4** LSVs measured at 1 mV $s^{-1}$ of commercial $IrO_x$ in different electrochemical setups. The SPEC-XAS cell consists of the iridium oxide spray coated onto a Au/PTFE substrate to a loading of 0.19 ± 0.01 $mg_{Ir}$ $cm^{-2}$ and is measured under constant $N_2$ purging at 50 ml $min^{-1}$ with a 1 M $H_2SO_4$ electrolyte flowing continuously at 4 ml $min^{-1}$. The FE has the iridium oxide vacuum deposited onto a Au/PCTE substrate with an iridium loading of 0.016 $mg_{Ir}$ $cm^{-2}$ and static 1 M $H_2SO_4$ electrolyte.

The Ir $L_{III}$ edge spectra were collected in QEXAFS (Quick EXAFS) mode during 30-minute potential holds and the resulting merged XANES (X-ray absorption near edge structure) spectra shown in Figure 5. The iridium white line at 11,215 eV arises from the dipole allowed transitions of 2p to 5d states. Comparison of

the spectra shows the oxidation and reduction of the iridium oxide as a function of potential. Using the SPEC-XAS cell, high quality XAS data were collected at higher potentials and higher current densities than previously reported. The recorded mass activity over the 30-minute holds of XAS acquisition are shown in Figure S7. Stable currents in excess of 0.35 A $mg_{Ir}^{-1}$ were recorded while collecting XAS spectra (the time resolved XANES for the *iR* corrected holds at 1.72 and 1.85 V are shown in Figure S9). The XANES are shifting to higher values as the electrode is being oxidised.

Recent publications have shown the formation of Ir(V) at OER potentials and suggest that its formation is essential for OER onset.[18, 25-27] There are also two redox transitions occurring during the cyclic voltammogram , $Ir^{3+} \rightarrow Ir^{4+}$ and $Ir^{4+} \rightarrow Ir^{5+}$ .[25] This is in agreement with the voltammetry (Figure S6) and the shift we observe in the white line. This 1.7 eV shift is a result of the different cumulative proportions of $Ir^{3+}$, $Ir^{4+}$ and $Ir^{5+}$ present at each potential. During the OER the XANES is shifted to the highest values due to the formation of $Ir^{5+}$.

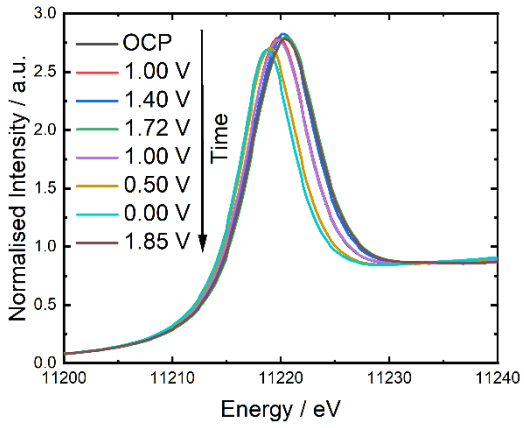


**Figure 5** Ir $L_{III}$ edge XANES of the electrode shown in Figure 4 measured during 30-minute chronoamperometric holds (Figure S7) in flowing 1 M $H_2SO_4$ (4 ml $min^{-1}$) under $N_2$ purging at 50 ml $min^{-1}$. All measurements were performed on the same electrode consecutively with the potentials quoted in the order they were run and *iR* corrected.

Analysis of the EXAFS data is important to understanding the structural changes occurring during this oxidation state change. The EXAFS *χ(k)* and Fourier transform plots are shown in Figure S10. The quality of the *χ(k)* data is important for accurate EXAFS analysis, the *χ(k)* data presented a good signal to noise ratio up to 12 $Å^{-1}$. The Au $L_{III}$ absorption edge is at 11919 eV at which we see a small absorption edge from the Au current collector. This limits the data collection to an energy range of around 11,010 to 11,900 eV; however, this is enough for multiple shell EXAFS fitting.

### $CO_2$RR on Oxide-Derived Copper

The electrochemical $CO_2$ reduction reaction is a gas consuming and gas producing reaction also chosen to demonstrate the quality of XAS data which can be achieved in the SPEC-XAS cell under high mass transport conditions. Figure 6 shows a potential hold at OCP, -0.34 V and -1.25 V vs. RHE with two samples taken during each potential hold with a 15-minute separation under $CO_2$RR conditions in the SPEC-XAS cell. A CuO catalyst spray coated onto the Au coated PTFE membrane was employed as the working electrode. During the -0.34 V vs. RHE hold the CuO is observed to reduce to Cu metal before the onset of $CO_2$ reduction. The -1.25 V hold reaches a mass activity of -0.1 A $mg_{Cu}^{-1}$ (sufficient to reduce $CO_2$), with the major products being carbon monoxide, ethylene, and hydrogen. Note that the Au is also a good $CO_2$ reduction catalyst having a high selectivity for carbon monoxide. There is therefore some contribution in the carbon monoxide Faradaic efficiency from the gold current collector reacting with the $CO_2$. However, the formation of ethylene occurs almost exclusively on copper-based catalysts and is therefore a good indication that the CuO-derived catalyst is doing $CO_2$RR to ethylene. Additionally, during this potential hold, the fractions of products increased over time. This suggests that the gas mixture reaching the GC has not reached equilibrium due to the large volume of the gas side (necessary for fluorescence windows and variable incidence angles). At the 50 ml $min^{-1}$ $CO_2$ flow rate used, it would take approximately 33 minutes to reach equilibrium, with the two samples taken during $CO_2$RR measured after 5 and 20 minutes. Importantly, the formation of ethylene is observed, although only small fractions, this validates the use of the cell for the study of the electrocatalyst during $CO_2$ reduction.

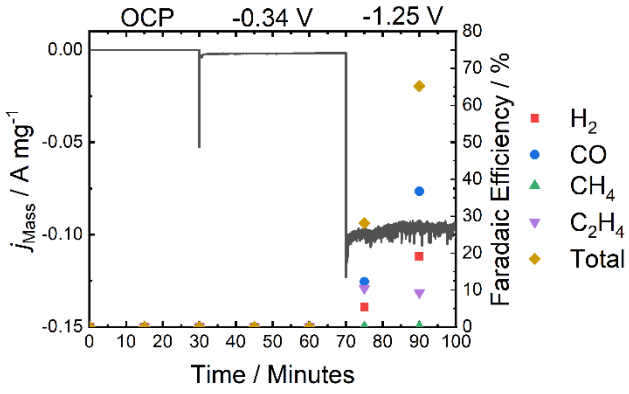


**Figure 6** Chronoamperometric response and the corresponding Faradaic efficiency for the different reduction products measured using *in situ* gas chromatography of a CuO catalyst spray coated onto a Au/PTFE substrate (0.40 ± 0.01 $mg_{Cu}$ $cm^{-2}$). The cell was configured as in Figure S11a, with a 1 M $KHCO_3$ electrolyte at a flow rate of 5 ml $min^{-1}$ and a $CO_2$ flow rate of 50 ml $min^{-1}$ using a platinum mesh counter electrode and a Leak-Free Ag/AgCl reference electrode (Alvatech). Both potentials are *iR* corrected and converted to RHE.

The *in situ* Cu K edge XANES is shown in Figure 7 measured at OCP, - 0.34 V and -1.25 V vs. RHE. At OCP, the catalyst is bulk CuO, showing the characteristic pre-peak between 8976-8979 eV which arises from dipole-forbidden 1s→3d electronic transition and the shoulder at 8985-8987 eV that arises from the 1s→4p transition. The -1.25 V spectra, when $CO_2$ reduction is occurring, shows the copper in its fully reduced state, $Cu^0$. The spectrum taken 15 minutes into the -0.34 V hold shows

a majority of $Cu^0$ but with some of the oxide remaining. This is also visible in the Fourier transform (Figure S14b) where a small peak for Cu-O coordination is still present. The relatively large crystallite size of the copper (18 nm by XRD, Figure S15) will create a delay in reducing the bulk of the copper. Therefore, the residual oxygen is likely confined to the core of the metal oxide particles and at longer times and more reducing potentials, the bulk fully reduces.[28]

High quality EXAFS were collected during the reaction (shown in Figure S14) under high gas evolution conditions. This is an improvement upon previous cell designs where when used for $CO_2$ reduction testing, -0.75 V vs. RHE was the lowest potential achieved before interference with bubbles. [16, 29] In these earlier reports the cell designs didn't have a gas feed directly to the working electrode, and mass transport was therefore limited by the solubility of $CO_2$ in the electrolyte. We have demonstrated good data quality down to -1.25 V vs. RHE.

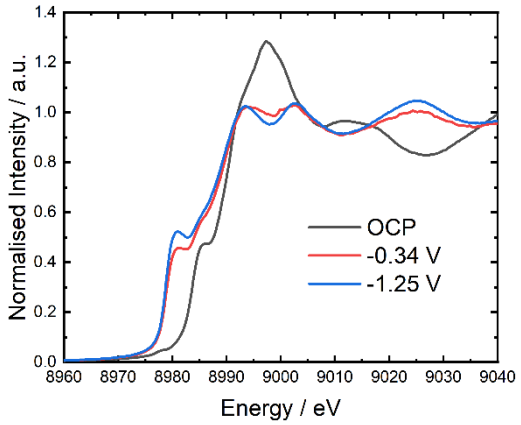


**Figure 7** Cu K edge XANES where the OCP and -1.25 V spectra are taken as the merge of all spectra acquired during the 30 minute potential holds (Figure S13). The data shown for -0.34 V is a singular spectrum taken after 15 minutes of the 40 minute hold and shows the partial reduction of the CuO. Measured in 1 M $KHCO_3$ at a flow rate of 5 ml $min^{-1}$ and a $CO_2$ flow rate of 50 ml $min^{-1}$ using a platinum mesh counter electrode and a Leak-Free Ag/AgCl reference electrode (Alvatech). Both potentials are *iR* corrected and converted to RHE.

## ORR on Platinum

The results of electrochemical testing for a 50% Pt/C catalyst with an electrode loading of 0.159 $mg_{Pt}$ $cm^{-2}$ are shown in Figure 8. The ORR was studied in 1 mol $dm^{-3}$ $H_2SO_4$ while scanning the potential at 100 mV $s^{-1}$ and with an oxygen partial pressure of 102 kPa. $H_2SO_4$ is more similar to the sulphonic group in Nafion™ and was therefore chosen for this study. A maximum mass activity of 1.26 A $mg_{Pt}^{-1}$ was achieved at 0.46 V (vs. RHE), which corresponds to a geometric current density of -193 mA $cm^{-2}$. Compared to the FE, this is approximately two orders of magnitude lower than the fully optimised electrode and is of comparable activity to electrodes untreated with Teflon AF.[22] By increasing the hydrophobicity of the catalyst layer with Teflon AF 2400, Lin et al. found the gas permeability at the catalyst surface is significantly increased, improving the mass transport and increasing the mass activity by two orders of magnitude.[22] The electrodes in this study only contain Nafion™ which is in contact with aqueous electrolyte as a 'hydrophilic' reservoir. This could create an oxygen concentration gradient through the thickness of the electrode which results in a corresponding gradient in reaction rate through the thickness of the electrode, which we are unable to quantify. Similarly, the relatively thick electrodes required by the XAS measurements result in some through plane resistance which may also contribute to the error in the *iR* corrected potential. These combined effects may be as much as ~70 mV (calculation in supporting information S4). Additionally, thickness effects may also affect the proton conductivity through the electrode, this will be discussed below. Further improvement in the activity of the electrodes may be possible with optimisation of the hydrophobicity of the catalyst layers. In the literature it is more common to compare the ORR activity of different catalysts in PEM fuel cells or gas diffusion electrodes using the kinetically controlled current density (where mass transport is negligible), typically 0.9 V. At this potential, the anodic scan has a current density of 18 mA $mg_{Pt}^{-1}$, slightly lower than the 60 °C literature reported values between 20 - 25 mA $mg^{-1}$ also in 1 M $H_2SO_4$.[30] The difference in activity between the SPEC-XAS cell and the literature reported values can therefore be accounted for by this temperature difference.

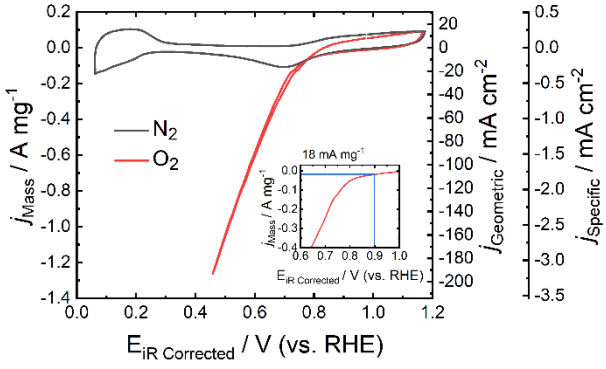


**Figure 8** Cyclic voltammograms measured at 100 mV $s^{-1}$ of the Pt/C (0.15 ± 0.02 $mg_{Pt}$ $cm^{-2}$) on Pd/PTFE electrodes in the SPEC-XAS cell under $N_2$ and $O_2$ purging at 50 ml $min^{-1}$ with a 1 M $H_2SO_4$ electrolyte flowed at 4 ml $min^{-1}$ continuously. Inset shows a zoomed in area of the capacitance corrected kinetically controlled region of the electrode during ORR. Before and after testing cyclic voltammograms shown in Figure S17.

The Pt $L_{III}$ edge spectra were collected during potential holds of 20 minutes in both oxygen and nitrogen. The maximum current density at which the XAS was measured was approximately -1.20 A $mg_{Pt}^{-1}$ during the ORR, Figure 10. Two potentials (-0.05 and -0.09 V vs. RHE) were also measured during the hydrogen evolution reaction (HER) under nitrogen, reaching -0.30 A $mg_{Pt}^{-1}$. Spectra were measured in QEXAFS mode with a scan collected approximately every 120 seconds. The resulting merged XANES spectra are shown in Figure 9.

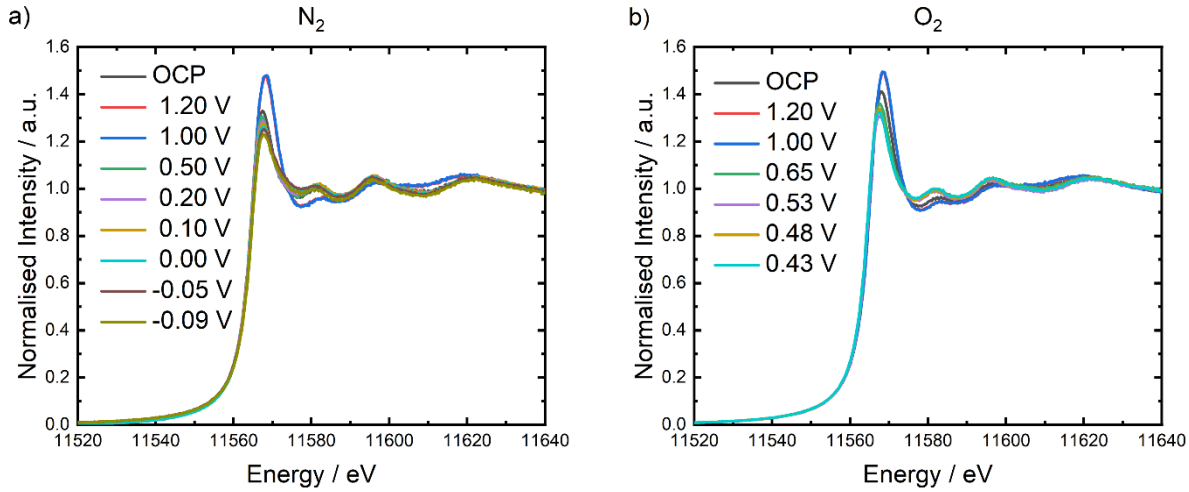


**Figure 9** Pt $L_{III}$ edge XANES measured during chronoamperometric holds (Figure S18) in flowing 1 M $H_2SO_4$ (4 ml $min^{-1}$) under $N_2$ (a) and $O_2$ (b) purging at 50 ml $min^{-1}$.

The same potential profiles were used for both oxygen and nitrogen (Figure S19) and the *iR* corrected potentials are quoted in the order in which they were measured. The Pt $L_{III}$ X-ray absorption edge arises from the transition of the 2p J=3/2 core states to unoccupied 5d states. Therefore, the area under the white line correlates with the density of the unoccupied 5d states.[31] Analysis of the XANES region reveals a broadening of the white line in nitrogen as hydrogen is adsorbed and during hydrogen evolution (<0 V, this is shown in Figure S21). Such broadening has been observed before and has been attributed to transitions of electrons in the Pt-H antibonding orbitals.[32-33]

Quantitative determination of the number of unoccupied 5d states requires comparison of both the $L_{II}$ and $L_{III}$ spectra as described by Mansour et al.[34]. However, quantitative comparisons can be made by integrating the area under the white line as is common on other metal $L_{III}$ edges.[35] Increases in d-band vacancies mainly arise from electrochemical oxidation of Pt and oxygen adsorption with subsequent electron donation from the Pt. The background of the XANES was fitted with an arctangent function and the white line fit using a Lorentzian function. The area was taken as the integral of the Lorentzian peak, the fitted areas are shown in Figure 10 for both oxygen and nitrogen environments as a function of potential (fits are shown in Figures S23 and S24).[36] Figure 10 shows that over all potentials in oxygen the area of the white line is larger than in nitrogen by up to 1.06 times, suggesting more oxidation of the platinum in oxygen than in nitrogen. Even at oxidising potentials, the sample in nitrogen has a lower effective oxidation state than in oxygen. This effect was also observed by Erickson et al. who attributed it to the physisorption of $O_2$ as the platinum oxide reduction peak in the cyclic voltammogram didn't increase between $N_2$ and $O_2$ purging.[36] However, physisorption of $O_2$ on platinum is unlikely to change the Pt electronic structure enough to be visible in the XANES spectra.

There is a progressive oxidation of the platinum during the oxidative hold at 1.2 V in both $N_2$ and $O_2$. This can be seen in the time resolved XANES spectra (Figure S24 and Figure S26) at 1.2 V vs. RHE and a corresponding increase in the fitted white line areas (Figure S25 and Figure S27) over the 20-minute hold. The change in the extent of oxidation compared to that at OCP is greater in $N_2$ than $O_2$, having an area difference of 1.7 and 1.1 for $N_2$ and $O_2$, respectively. However, this arises from the lower potential at OCP in $N_2$ which corresponds to a starting point which is more reduced with a smaller white line area. At OCP in $O_2$ the platinum surface should be oxidised due to the formation of PtO.[37] During the subsequent 1 V vs. RHE hold the peak area remains constant suggesting no further oxidation.

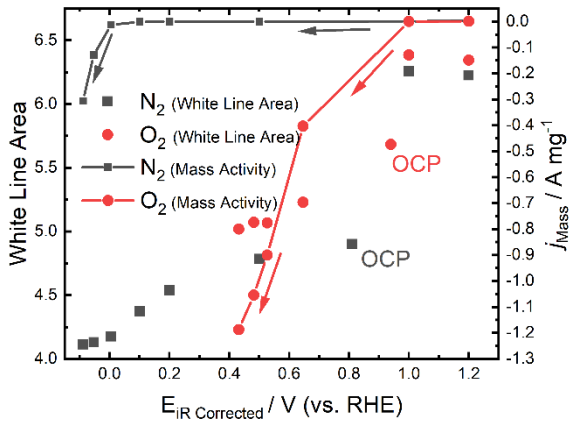


**Figure 10** Areas of the fitted Lorentzian functions at the Pt $L_{III}$ edge as a function of potential in $O_2$ and $N_2$. Corresponding fits are shown in Figures S23 and S24. Also shown is a steady state voltammogram calculated from the average of the current measured during the 20-minute potential holds of XAS acquisition scanning in the cathodic direction.

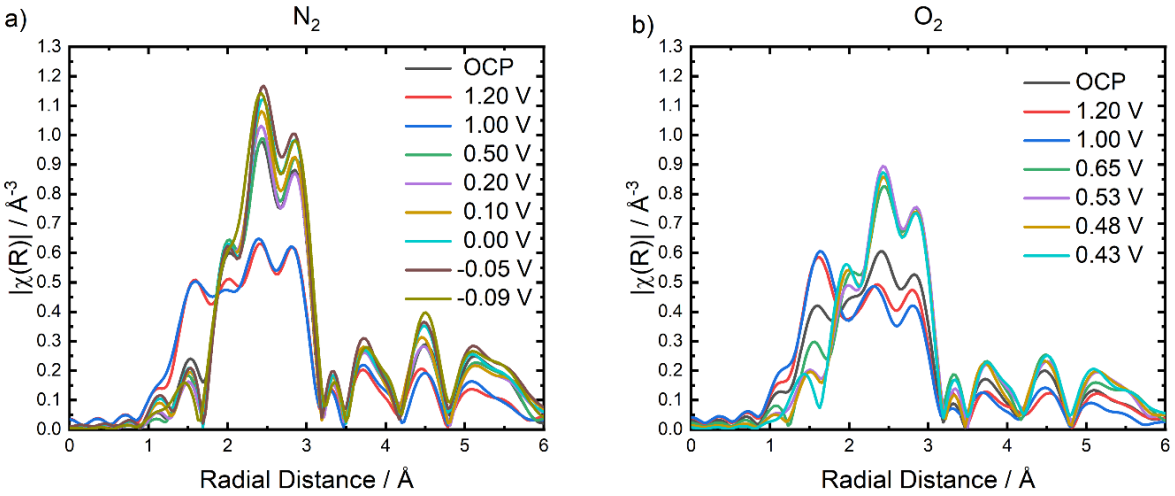


**Figure 11** Fourier transform of the $k^2$ weighted Pt-$L_{III}$ EXAFS (not phase corrected) of 50% Pt/C catalyst at different potentials under $N_2$ (a) and $O_2$ (b) saturated electrolyte. Corresponding $\chi(k)$ data is shown in Figure S29.

By using the $\Delta\mu$ method the surface and subsurface speciation can be investigated.[38-40] This method removes the bulk XANES by subtraction of the unreactive interior Pt atoms. To do this, the XANES of Pt in the double layer region (where there is minimal interaction with oxygen or hydrogen) is subtracted from the spectra at different potentials:

$$\Delta\mu = \mu(V, N_2 \text{ or } O_2) - \mu(0.50\ V, N_2)$$

The resulting difference plots are shown in Figure S28. The small negative peaks at around 11,565 eV are associated with subsurface oxygen, while the large main peaks around 11,570 eV ascribed to surface oxygen.[40] As shown by Kongkanand and Ziegelbauer, when in $N_2$, these subsurface oxygen peaks aren't visible, even when applying an oxidising potential.[38] In oxygen however, at OCP, 1.20 V and 1.00V, subsurface oxygen appears to be present. The size of this peak doesn't change upon application of an oxidising potential, suggesting that the subsurface oxygen is already present following the CVs used to clean the electrode. The OCP in $O_2$ remained higher than in $N_2$ after these CVs because of a higher degree of oxidation, the OCP in $N_2$ decreased significantly more. The main difference observed between OCP and 1.20 or 1.00 V is the increase in the surface oxygen peak. This peak also remains present at ORR potentials, correlating with the observation that the white line area remains larger in oxygen compared to nitrogen (Figure 10) as the amount of oxygen on the surface of the electrode is larger.

The speciation of platinum can further be evaluated by analysing the EXAFS collected at each potential (Figure 11). The Fourier transform of the experimental EXAFS was fitted using a constrained version of the model published by Frenkel et al. (Table S1).[41]The resulting fits are shown in Figure S30 and Figure S31 and results for each fit are presented in Tables S2 and S3. The main changes observed are the first shell Pt-Pt and Pt-O coordination shells. These differences are presented in Figure 12. In nitrogen, the Pt-Pt coordination is unchanged apart from when applying oxidising potentials, where Pt-O bonds are forming. The Pt-Pt coordination decreases as the bonds are breaking due to oxide formation. The removal of all the oxygen neighbours under nitrogen when the potential is reduced to ≤ 0.5 V shows that all the sites within the catalyst layer are in electrochemical contact. In oxygen the Pt-Pt coordination is reduced by approximately 1.2 (at 0.5 V vs. RHE) during the ORR compared to an inert atmosphere. The Pt-Pt coordination at oxidising potentials is also significantly lower than in nitrogen. The results indicate that during ORR some of the oxide remains on the surface, either as an intermediate in the reaction or as a remaining passivation layer. At these potentials in nitrogen there are no oxygen neighbours remaining, this demonstrates that the electrode can be fully reduced. This effect is therefore caused by the presence of oxygen and is not the result of poor proton conductivity through the catalyst layer. Retention of these oxygen neighbours persists down to 0.48 V (vs. RHE), well below the platinum oxide reduction peak.

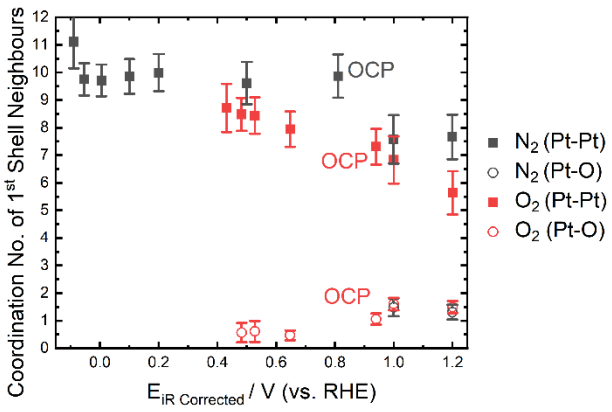


**Figure 12** First shell coordination numbers for the Pt-Pt shell and Pt-O shell as a function of the potential.

## Conclusion

A spectro-electrochemical cell for *in situ* XAS measurements of gas evolving and consuming reactions at synchrotron X-ray sources was developed and commissioned. The electrolyte and gas flow paths coupled with porous gas diffusion electrodes ensure homogeneous experimental conditions and wider range of potentials over which XAS spectra can be collected. In this report, the cell has been used to study the OER, $CO_2$RR and ORR at high overpotentials and it can be further applied to the study of other electrochemical reactions or other synchrotron X-ray techniques such as high energy resolution fluorescence detection (HERFD) XANES, $k_\alpha$ and $k_\beta$ X-ray emission spectroscopy (XES) and valence to core transitions.

The ability of the SPEC-XAS cell in characterising gas evolving and consuming reactions at elevated current densities has been demonstrated on a highly active iridium oxide electrocatalyst during the OER and copper oxide during the $CO_2$RR. Iridium oxide has been studied at a range of potentials, reaching a maximum current density of 0.35 A $mg_{Ir}^{-1}$ during *in situ* oxygen evolution measurements. The potential dependent shift of the iridium white line along with the good quality EXAFS data shows the applicability of the cell in characterising highly active electrocatalysts during strong gas evolving conditions. Through inline gas chromatography, the applicability of the cell in characterising $CO_2$RR catalysts has also been demonstrated. These GC measurements show the main $CO_2$ reduction product to be carbon monoxide along with a detectable amount of ethylene (~10% Faradaic efficiency). The *in situ* XANES and EXAFS data show the catalyst is fully reduced to $Cu^0$ at potentials at which $CO_2$ reduction occurs, with no detectable oxide remaining. However, the bulk sensitivity of XAS limits the detection of surface species due to the relatively large particle sizes.

Finally, we have conducted an in-depth study of the platinum speciation under a range of oxidising and reducing conditions, to understand and investigate the presence of oxygen on the surface and subsurface during the ORR. Using the white line areas, the $\Delta\mu$ technique and the EXAFS data it was observed that when an oxidising potential is applied, a mixture of subsurface and surface platinum oxide is present. During the ORR, some of the oxygen remains on the surface which is fitted as a Pt-O shell in the EXAFS analysis. The oxygen during the ORR is confined to the surface and with no detectable oxygen remaining in the subsurface.

## Experimental Section

### Preparation of Electrodes

Working electrodes were prepared by spray coating the catalyst ink suspension onto a Au (for iridium and copper measurements) or Pd (for platinum measurements) coated PTFE substrate to a geometric area of 3.14 $cm^2$ using a stencil. The Au coated PTFE substrate was prepared by sputtering a Au layer (100 nm) onto a PTFE membrane (Fisherbrand™, 0.45 µm, 47 mm). The Pd coated PTFE substrate was prepared by PVD of a Pd layer (100 nm) onto the PTFE membrane.

The iridium oxide ink suspension consisted of a Premion™ $IrO_x$ (Alfa Aesar) catalyst, Milli-Q $H_2O$, IPA and 5 wt.% Nafion™ ionomer solution. The XRF loading of the electrode used for *in situ* XAS measurements is 0.19 ± 0.01 $mg_{Ir}$ $cm^{-2}$.

The copper oxide ink consisted of a CuO (Johnson Matthey) catalyst, Milli-Q $H_2O$, IPA and 10 wt.% Nafion™ ionomer solution. The XRF loading of the electrode used for *in situ* XAS measurements is 0.40 ± 0.01 $mg_{Cu}$ $cm^{-2}$.

The platinum ink consisted of a 50% Pt/C (Johnson Matthey) catalyst, Milli-Q $H_2O$, IPA and 5 wt.% Nafion™ ionomer solution. The XRF loading of the electrode used for *in situ* XAS measurements is 0.15 ± 0.02 $mg_{Pt}$ $cm^{-2}$.

### *In situ* XAS Setup

Electrochemical measurements of the iridium oxide were conducted in a 1 M $H_2SO_4$ electrolyte at a flow rate of 4 ml $min^{-1}$ and all gas flow rates were kept at 50 ml $min^{-1}$. A platinum mesh and an RHE (Hydroflex, Gaskatel™) were used as the counter and reference electrodes respectively. The working electrode was cycled at 100 mV $s^{-1}$ between 0 and 1.35 V vs. RHE in $N_2$ before any XAS measurements were taken. Firstly, XAS spectra were collected in nitrogen at OCP, then successively 30-minute chronoamperometric holds were taken at (1.0 V, 1.4 V, 1.8 V, 1.0 V, 0.5 V, 0.0 V, 2.0 V). The spectra collected during each potential hold were averaged to yield one XAS spectrum per potential.

$CO_2$RR measurements on copper oxide were conducted in a 1 M $KHCO_3$ electrolyte at a flow rate of 5 ml $min^{-1}$ and all gas flow rates were kept at 50 ml $min^{-1}$. A platinum mesh and a Leak-Free Ag/AgCl reference electrode (LF-5, Alvatek) were used as the counter and reference electrodes respectively. Firstly, XAS spectra were collected in carbon dioxide at OCP, then successively chronoamperometric holds were taken at (-1.0 V, -1.91 V vs. Ag/AgCl). All applied potentials were converted to the RHE by the equation: E (vs. RHE) = E (vs. Ag/AgCl) + 0.204 V + 0.0591 V × pH – iR) and a pH of 7.8.

Measurements at the platinum edge were conducted in a 1 M $H_2SO_4$ electrolyte at a flow rate of 5 ml $min^{-1}$ and all gas flow rates were kept at 50 ml $min^{-1}$. A platinum mesh and an RHE (Hydroflex, Gaskatel™) were used as the counter and reference electrodes respectively. The working electrode was cycled at 100 mV $s^{-1}$ between 0.0 and 1.0 V vs. RHE in $N_2$ before any XAS measurements were taken. Firstly, XAS spectra were collected in oxygen at OCP, then successively 20-minute chronoamperometric holds were taken at (1.2 V, 1.0 V, 0.5 V, 0.2 V, 0.1 V, 0.0 V). This was repeated for $N_2$ with additional measurements at -0.1 V and -0.2 V. The spectra collected during each potential hold were averaged to yield one XAS spectrum per potential.

### Gas Chromatography during the $CO_2$RR

The $CO_2$RR performance was evaluated in the SPEC-XAS connected to a GC calibrated for four standard gasses ($H_2$, CO, $CH_4$ and $C_2H_4$). The setup was kept the same as the *in situ* XAS measurements for consistency. Gas samples were taken from the

outlet gas stream of the cell every 15 minutes. The Faradaic efficiency is calculated from the partial current density ($j_{product}$) divided the total current density ($j_{total}$):

$$j_{product} = \frac{n \times C \times Q_{flow} \times F}{V_m}$$

$$FE = \frac{j_{Product}}{j_{total}}$$

Where $n$ is the number of electrons transferred, $C$ is the concentration of gaseous product, $Q_{flow}$ is the volumetric flow rate, $F$ is the Faraday constant and $V_m$ is the molar volume of gas.

### XAS Characterisation

All XAS spectra were collected at the B18 beamline at Diamond Light Source using the fast scanning (QEXAFS) Si (111) double crystal monochromator and a 36 element Ge fluorescence detector. For Ir $L_{III}$ and Pt $L_{III}$ edge measurements X-ray energy calibration was done with a Pt reference foil to the Pt $L_{III}$ edge. For copper measurements, X-ray energy calibration was done with a Cu reference foil to the Cu K edge. For the Ir $L_{III}$ edge, each spectrum took approximately 40 s to acquire ($k_{max}$ = 13 Å$^{-1}$), Pt $L_{III}$ edge spectra took approximately 60 s to acquire ($k_{max}$ = 12 Å$^{-1}$), and Cu K edge spectra took approximately 35 s to acquire ($k_{max}$ = 13 Å$^{-1}$). Before each experiment the reference foil was measured to check beam drift correct with alignment.

### XAS Data Analysis

The Athena module of the Demeter software suite was used for the XAS data alignment, normalisation, and background subtraction.[42] The analysis of the Platinum EXAFS data was performed using the Artemis module. The Fourier transform k range was kept between 3-12 Å$^{-1}$ during fitting and a mixed k-weight factor was used to optimise the fit. An amplitude reduction factor of $S_0^2$ = 0.81 was calculated from the fitting of a Pt foil. This was then fixed during the fitting of all experimental data while the coordination number, bond distance, Debye-Waller factor and energy parameters were allowed to vary.

## Acknowledgements

We thank Johnson Matthey, Diamond Light Source and EPSRC for providing funds for an iCASE PhD studentship. We are grateful to Diamond Light Source for provision of beamtime at B18 (NT35412-1 JM22931-9 & SP33009-1). We thank Johnson Matthey for supplying the CuO, Pt/C and $IrO_x$ catalysts. We thank Alan Glass (University of Southampton), Sam Embling (Diamond Light Source) and Phil Robbins (Diamond Light Source) for constructing the in-situ cell. We thank Nikolay Zhelev (University of Southampton) for collecting SEM images and Huw Marchbank (Johnson Matthey) for collecting and analysing XRDs.

**Keywords:** Electrochemistry • *in situ* XAS • ORR • OER • $CO_2$RR

[1] E. Fabbri, A. Habereder, K. Waltar, R. Kötz, T. J. Schmidt, *Catal. Sci. Technol.* **2014**, *4*, 3800-3821.
[2] C. C. L. McCrory, S. Jung, J. C. Peters, T. F. Jaramillo, *J. Am. Chem. Soc.* **2013**, *135*, 16977-16987.
[3] M. Clapp, C. M. Zalitis, M. Ryan, *Catal. Today* **2023**, *420*, 114140-114140.
[4] E. Antolini, *Appl. Catal., B* **2016**, *181*, 298-313.
[5] E. Antolini, *Mater. Chem. Phys.* **2003**, *78*, 563-573.
[6] H. Macpherson, T. Hodges, M. H. Chuma, C. Sherwin, U. Podbevšek, K. Rigg, V. Celorrio, A. E. Russell, E. C. Corbos, *Johnson Matthey Technol. Rev.* **2023**, *67*, 97-109.
[7] D. U. Nielsen, X.-M. Hu, K. Daasbjerg, T. Skrydstrup, *Nat. Catal.* **2018**, *1*, 244-254.
[8] K. P. Kuhl, E. R. Cave, D. N. Abram, T. F. Jaramillo, *Energy Environ. Sci.* **2012**, *5*, 7050-7059.
[9] M. Bogar, Y. Yakovlev, J. Nováková, A. M. Darabut, M. Kriechbaum, H. Amenitsch, R. Taccani, I. Matolínová, *Int. J. Hydrogen Energy* **2024**, *58*, 1673-1681.
[10] I. Martens, A. Vamvakeros, N. Martinez, R. Chattot, J. Pusa, M. V. Blanco, E. A. Fisher, T. Asset, S. Escribano, F. Micoud, T. Starr, A. Coelho, V. Honkimäki, D. Bizzotto, D. P. Wilkinson, S. D. M. Jacques, F. Maillard, L. Dubau, S. Lyonnard, A. Morin, J. Drnec, *ACS Energy Lett.* **2021**, *6*, 2742-2749.
[11] M. Ronovský, M. Myllymäki, Y. Watier, P. Glatzel, P. Strasser, A. M. Bonastre, J. Drnec, *J. Power Sources* **2024**, *592*, 233906.
[12] A. E. Russell, A. Rose, *Chem. Rev.* **2004**, *104*, 4613-4636.
[13] K. Liu, W. A. Smith, T. Burdyny, *ACS Energy Lett.* **2019**, *4*, 639-643.
[14] T. Binninger, E. Fabbri, A. Patru, M. Garganourakis, J. Han, D. Abbott, O. Sereda, R. Kötz, A. Menzel, M. Nachtegaal, T. Schmidt, *J. Electrochem. Soc.* **2016**, *163*, H906-H912.
[15] K. Sardar, E. Petrucco, C. I. Hiley, J. D. Sharman, P. P. Wells, A. E. Russell, R. J. Kashtiban, J. Sloan, R. I. Walton, *Angew. Chem., Int. Ed.* **2014**, *53*, 10960-10964.
[16] A. M. Wise, P. W. Richardson, S. W. T. Price, G. Chouchelamane, L. Calvillo, P. J. Hendra, M. F. Toney, A. E. Russell, *Electrochim. Acta* **2018**, *262*, 27-38.
[17] D. L. Burnett, E. Petrucco, A. E. Russell, R. J. Kashtiban, J. D. B. Sharman, R. I. Walton, *Phys. Chem. Chem. Phys.* **2020**, *22*, 18770-18773.
[18] N. Diklić, A. H. Clark, J. Herranz, D. Aegerter, J. S. Diercks, A. Beard, V. A. Saveleva, P. Chauhan, M. Nachtegaal, T. Huthwelker, D. Lebedev, P. Kayser, J. A. Alonso, C. Copéret, T. J. Schmidt, *ACS Catal.* **2023**, *13*, 11069-11079.
[19] N. Diklić, A. H. Clark, J. Herranz, J. S. Diercks, D. Aegerter, M. Nachtegaal, A. Beard, T. J. Schmidt, *ACS Energy Lett.* **2022**, *7*, 1735-1740.
[20] L. V. Bühre, A. J. McLeod, P. Trinke, B. Bensmann, M. Benecke, O. E. Herrera, W. Mérida, R. Hanke-Rauschenbach, *J. Electrochem. Soc.* **2023**, *170*, 094507-094507.
[21] C. M. Zalitis, D. Kramer, A. R. Kucernak, *Phys. Chem. Chem. Phys.* **2013**, *15*, 4329-4340.
[22] X. Lin, C. M. Zalitis, J. Sharman, A. Kucernak, *ACS Appl. Mater. Interfaces* **2020**, *12*, 47467-47481.
[23] T. Reier, M. Oezaslan, P. Strasser, *ACS Catal.* **2012**, *2*, 1765-1772.
[24] M. Bernt, H. A. Gasteiger, *J. Electrochem. Soc.* **2016**, *163*, F3179.
[25] A. Minguzzi, C. Locatelli, O. Lugaresi, E. Achilli, G. Cappelletti, M. Scavini, M. Coduri, P. Masala, B. Sacchi, A. Vertova, P. Ghigna, S. Rondinini, *ACS Catal.* **2015**, *5*, 5104-5115.
[26] H. N. Nong, T. Reier, H.-S. Oh, M. Gliech, P. Paciok, T. H. T. Vu, D. Teschner, M. Heggen, V. Petkov, R. Schlögl, T. Jones, P. Strasser, *Nat. Catal.* **2018**, *1*, 841-851.
[27] A. Minguzzi, O. Lugaresi, C. Locatelli, S. Rondinini, F. D'Acapito, E. Achilli, P. Ghigna, *Anal. Chem.* **2013**, *85*, 7009-7013.
[28] X. Wang, K. Klingan, M. Klingenhof, T. Möller, J. Ferreira de Araújo, I. Martens, A. Bagger, S. Jiang, J. Rossmeisl, H. Dau, P. Strasser, *Nat. Commun.* **2021**, *12*, 794-794.
[29] M. J. Lawrence, V. Celorrio, E. Sargeant, H. Huang, J. Rodríguez-López, Y. Zhu, M. Gu, A. E. Russell, P. Rodriguez, *ACS Appl. Mater. Interfaces* **2022**, *14*, 2742-2753.
[30] U. A. Paulus, T. J. Schmidt, H. A. Gasteiger, R. J. Behm, *J. Electroanal. Chem.* **2001**, *495*, 134-145.
[31] B. Qi, I. Perez, P. H. Ansari, F. Lu, M. Croft, *Phys. Rev. B* **1987**, *36*, 2972-2975.
[32] M. G. Samant, M. Boudart, *J. Phys. Chem.* **1991**, *95*, 4070-4074.
[33] J. McBreen, S. Mukerjee, *J. Electrochem. Soc.* **1995**, *142*, 3399-3404.
[34] A. N. Mansour, J. W. Cook, Jr., D. E. Sayers, *J. Phys. Chem.* **1984**, *88*, 2330-2334.
[35] D. J. Morris, P. Zhang, *Chem. Methods* **2021**, *1*, 162-172.
[36] E. M. Erickson, M. S. Thorum, R. Vasić, N. S. Marinković, A. I. Frenkel, A. A. Gewirth, R. G. Nuzzo, *J. Am. Chem. Soc.* **2012**, *134*, 197-200.
[37] U. Reimer, Y. Cai, R. Li, D. Froning, W. Lehnert, *J. Electrochem. Soc.* **2019**, *166*, F3098-F3104.
[38] A. Kongkanand, J. M. Ziegelbauer, *J. Phys. Chem. C* **2012**, *116*, 3684-3693.

[39] T. M. Arruda, B. Shyam, J. M. Ziegelbauer, S. Mukerjee, D. E. Ramaker, *J. Phys. Chem. C* **2008**, *112*, 18087-18097.
[40] M. Teliska, W. E. O'Grady, D. E. Ramaker, *J. Phys. Chem. B* **2005**, *109*, 8076-8084.
[41] A. I. Frenkel, C. W. Hills, R. G. Nuzzo, *J. Phys. Chem. B* **2001**, *105*, 12689-12703.
[42] B. Ravel, M. Newville, *J. Synchrotron Radiat.* **2005**, *12*, 537-541.